



Surface states of gas-atomized Al 6061 powders – Effects of heat treatment

Alexis T. Ernst^a, Peter Kerns^b, Aaron Nardi^c, Harold D. Brody^a, Avinash M. Dongare^a, Seok-Woo Lee^a, Victor K. Champagne^c, Steven L. Suib^{a,b}, Mark Aindow^{a,*}



^a Department of Materials Science and Engineering, Institute of Materials Science, University of Connecticut, Unit 3136, 97 North Eagleville Road, Storrs, CT 06269-3136, USA

^b Department of Chemistry, University of Connecticut, 55 North Eagleville Road, Unit 3060 Storrs, CT 06269-3060, USA

^c U.S. Army Research Laboratory, Weapons and Materials Research Directorate, Aberdeen Proving Ground, Aberdeen, MD 21005, USA

ARTICLE INFO

Keywords:

Aluminum alloy powder
Electron microscopy
Heat treatment
Surface oxide layer
X-ray photoelectron spectroscopy

ABSTRACT

Surface oxides formed on powder feedstocks used for cold spray deposition can play an important role in the bonding of the particles and in the development of defects in the deposit. A combination of scanning transmission electron microscopy and x-ray photoelectron spectroscopy was used to investigate the oxides formed on gas-atomized Al 6061 alloy feedstock powders. The powders were studied in the as-atomized condition and after two different thermal exposures that correspond to typical feedstock pre-treatment conditions. The surface features and internal microstructures are consistent with those reported previously for these powders. The as-atomized powders have 5.2 nm thick amorphous oxide layers, with an outer Mg-rich sub-layer and an inner Mg-lean sub-layer. Powders heat-treated at 230 °C in air exhibit slightly thicker oxide layers with a crystalline MgAl₂O₄ spinel outer sub-layer and an amorphous aluminum oxide inner sub-layer. Powders homogenized under Ar at 400 and 530 °C have significantly thicker (8.9 nm) oxide layers with evidence for a defect inverse spinel Al(Mg,Al)₂O₄ inner sub-layer between the MgAl₂O₄ spinel outer sub-layer and the alloy. Differences between these observations and those reported previously for oxidation of bulk alloys are explained on the basis of Mg surface segregation during the gas atomization process.

1. Introduction

The production of metal powders by atomization from the melt has been a standard approach to obtain feedstocks for conventional powder metallurgy (PM) processes [1], and has gained increased importance with the advent of metal additive manufacturing (MAM) [2,3]. A common concern with such powders is the surface condition, and in particular the thickness and character of any surface oxide layer that forms on the powder during the atomization process [4]. The volume fraction of such oxides can be significant, particularly for water-atomized powders [5,6], and a pre-consolidation reduction heat treatment is sometimes required to ensure adequate bonding between particles in PM processing [7,8] or to avoid excessive inclusion formation in MAM [9,10].

The role of the surface oxide is particularly critical for aluminum alloy powders, which are usually produced by gas atomization under inert gas cover [11,12]. Aluminum-based powders also form the basis for many energetic propellants, and the formation of a passivating oxide layer is essential if spontaneous ignition and combustion is to be avoided [13]. It is for this reason that a gas with a low oxygen partial

pressure is typically bled into the chamber at the end of an atomization run to allow the passivating layer to form before the powder is extracted from the cyclones. The role of the passivating layer in PM compacts of aluminum alloys and composites is complex; this can depend on the level of moisture and/or dissolved hydrogen involved, and on the resultant formation of hydroxides as opposed to (or in addition to) simple oxides [14,15]. The formation of hydroxides on Al powders has been demonstrated at room temperature in the presence of water vapor; the oxidation reaction products are aluminum oxide and varying concentrations of hydrated Al oxide incorporated into an amorphous surface film [16]. Subsequent to gas atomization, exposure to high temperature during the cold spray process, and/or to humidity (50% RH or higher) at room temperature during powder packaging, handling and storage, can contribute to further growth of the surface films. Such issues can be avoided to some extent by using high purity master alloys and processes such as gas atomization reaction synthesis (GARS), but the powder must then be consolidated promptly or stored carefully if hydroxides are not to develop by adsorption of atmospheric moisture [15,17].

Surface oxide layers play a specific role in gas dynamic cold spray

* Corresponding author.

E-mail address: m.aindow@uconn.edu (M. Aindow).

(GDCS) MAM of Al alloys. In GDCS, micron-sized particles are accelerated to supersonic velocities through a De Laval rocket nozzle using a heated high-pressure gas [18–20]. Above a certain critical velocity, the particles consolidate upon ballistic impingement with a suitable substrate surface [21,22]. The magnitude of the critical velocity can be estimated through the use of empirical relationships, which generally depend on particle material characteristics, such as density, ultimate strength, yield and melting point, as well as the particle temperature [23]. The formation of a metallurgical bond between the particle and the substrate depends on the magnitude of the pressure waves, with the associated softening and jet formation, all of which can be affected by the nature and thickness of the oxide layer that must be disrupted for bonding to occur [24–32].

In recent work, we have studied the GDCS of gas-atomized Al 6061 powder in the as-atomized condition and after two different post-atomization thermal exposures [33]. Low coverage cold spray deposits were produced from these powders to allow individual splats to be investigated. The microstructures of the powders and splats were investigated by electron microscopy, and the mechanical behavior of the particle/splat interiors were evaluated by compression and tension testing performed on micropillars milled from the samples [33,34]. A strong correlation was established between the microstructures of the powders and the deformation responses of the splat interiors. Here we consider the surface state of the same powders, with particular emphasis on the thickness, character and cation distribution in the corresponding oxide layers. By using a combination of scanning transmission electron microscopy (STEM) and X-ray photoelectron spectrometry (XPS) techniques, it is shown that there are fundamental differences in the surfaces of the powders in the three heat-treatment conditions. The consequences of these observations for the bonding of such particles during GDCS is discussed.

2. Materials and methods

All experiments were performed using gas-atomized Al 6061 powder obtained from Valimet, Inc. The powders were screened and classified to give particles with diameters of approximately $40 \pm 10 \mu\text{m}$. The powders were examined in the as-received condition and after two different thermal exposures that correspond to typical pre-treatment conditions for GDCS of Al 6061. The first of these is designated the “heat-treated condition” in which the powder was heated to a temperature of 230°C in laboratory air, held for 75 min, removed from the furnace and then allowed to cool to room temperature. The second of these is designated the “homogenized condition” since the process corresponds to the homogenization heat treatment for bulk Al 6061. In this process the powder was placed in a custom retort under an argon atmosphere to prevent excessive oxidation of the powder surface. The retort was ramped to 400°C and held for 2 h, then ramped to 530°C and held for 30 min, and then cooled rapidly to room temperature by quenching the sealed retort into ice water.

For electron microscopy studies, powder particles were attached to Al stubs using colloidal graphite and were firstly examined in an FEI Helios Nanolab 460F1, dual-beam gallium-ion focused ion beam (FIB) scanning electron microscope (SEM). Secondary electron (SE) SEM images of the powder surface morphologies were acquired using an accelerating voltage of 10 kV on the electron column. Suitable particles were then selected for examination by cross-sectional transmission electron microscopy (TEM). The TEM specimens were produced by FIB lift-out of lamellae cut from the region of interest (ROI). The powder particle surfaces were protected by depositing a strap of Pt across the ROI. This was performed in two steps: firstly, a layer of about 500 nm in thickness was deposited using the electron beam to crack the organometallic precursor; then a second layer, several microns in thickness, was deposited using the gallium ion beam. Since conventional trench milling of the particles led to rather unstable lamellae, and a high failure rate in specimen preparation, a circle-milling approach was

adopted. This method has been described in detail elsewhere [35] and involves milling semi-circular trenches on either side of the Pt strap so that the resultant parallel-sided lamella is supported by an annulus of metal prior to the lift-out step. The FEI Helios Nanolab 460F1 is equipped with a flip-stage for improved final thinning; the pre-thinned lamellae were lifted out and transferred onto Cu-omni grids on the flip-stage, and final thinning was performed by reducing the ion beam current iteratively to 24 pA. These specimens were analyzed in a FEI Talos F200X equipped with a Super-X silicon drift detector energy dispersive X-ray spectrometry (EDXS) system; the data were acquired at an operating voltage of 200 kV in STEM mode. The character of the surface layer on the powder particles was assessed by acquiring both EDXS line scans to measure compositional profiles and EDXS spectrum images to reveal the spatial distributions of the various species present in the specimens.

Further details about the chemical environments of the species at the surface of each type of powder were obtained using X-ray photoelectron spectroscopy (XPS). The XPS experiments were performed using a PHI model Quantum 2000 spectrometer with scanning ESCA multiprobe (Φ Physical Electronics Industries Inc.), using Al K α radiation ($\lambda = 1486.6 \text{ eV}$) as the radiation source. The spectra were recorded in the fixed analyzer transmission mode with pass energies of 187.85 eV and 29.35 eV for recording survey and high-resolution spectra, respectively. The powder samples were pressed on a double-sided carbon tape mounted on an Al coupon pinned to a sample stage and then introduced into the ultra-high vacuum chamber. Due to the sample geometry, the powders were examined in their native state (i.e., without Ar-ion sputtering). High resolution binding energies (BE) were measured for Mg 1s, Al 2p, and O 1s. The XPS spectra obtained were analyzed and fitted using CasaXPS software (version 2.3.16). Sample charging effects were eliminated by correcting the observed spectra with the C 1s BE value of 284.8 eV. To avoid errors in measured BE values due to possible shifts in the C 1s peak, the Au 4f_{7/2} (83.8 eV) peak from an internal calibration standard was used as a reference point. Five commercial reference standards were also analyzed using XPS as a basis for comparison with the data from the Al 6061 powder samples. These reference samples were: polycrystalline Al 6061 sheet in the T6 condition; single crystal substrates of MgO (rocksalt structure), MgAl₂O₄ (spinel) and α -Al₂O₃ (sapphire); and γ -Al₂O₃ powders. All of the reference samples except the γ -Al₂O₃ powders were cleaned by Ar-ion sputtering prior to analysis.

3. Results

3.1. Electron microscopy

A representative selection of SE-SEM micrographs obtained from the powder surfaces is shown in Fig. 1. While the powder particles were approximately spherical with diameters of $30\text{--}50 \mu\text{m}$, in all cases there were much finer satellites ranging in diameter from 0.2 to $5.0 \mu\text{m}$ attached to the surfaces. There were also pronounced ripples and grooves on the surface of the main particles (although not on the surfaces of the finer satellites). An example of an as-atomized particle that exhibits all these features is shown in Fig. 1a. There were no obvious differences in the surface features observed on the as-atomized, heat-treated or homogenized powders, and an example of a higher-magnification detail of a particle from each condition is shown in Fig. 1b-d, respectively. In each case, the surface grooves delineate approximately equiaxed patches around $2 \mu\text{m}$ across, with occasional ripples within these patches, and satellites attached to the surface.

The origins of the surface grooves are revealed in bright field STEM images obtained from FIB-cut cross-sections of the powders, and examples of such images are presented in Fig. 2. The as-atomized powder exhibits a cellular-dendritic microstructure with cells of around $2 \mu\text{m}$ in diameter delineated by a thin film of secondary phases (Fig. 2a). As shown previously [33], the cells consist of face-centered-cubic (FCC) Al

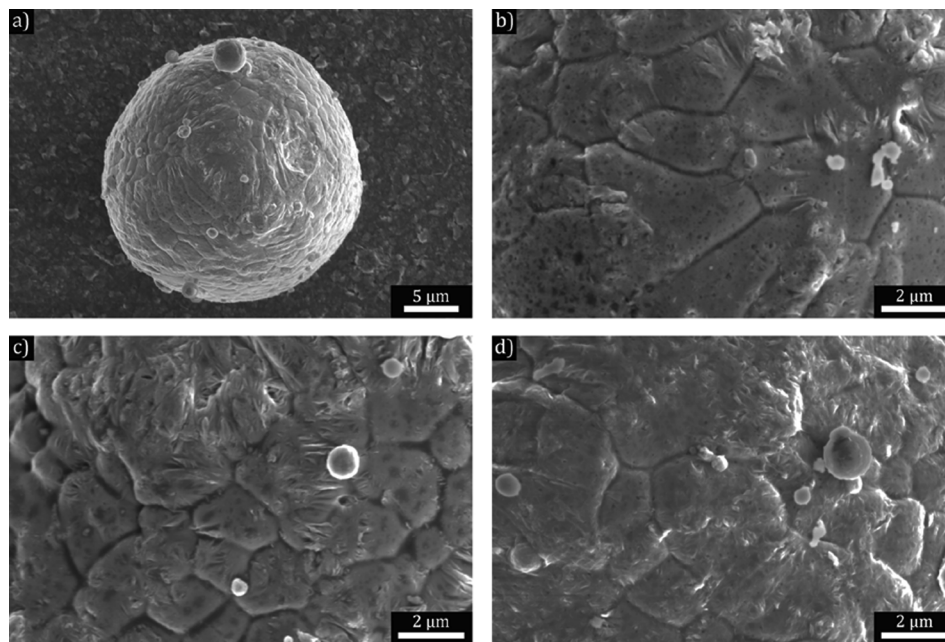


Fig. 1. SE-SEM micrographs of gas-atomized Al 6061 alloy powder surfaces: a) Low magnification image of a typical as-atomized powder particle; b)-d) higher magnification views of surface details on as-atomized, heat-treated, and homogenized powder particles, respectively.

supersaturated in Mg, with Mg- and Fe-rich silicide phases at the cell and grain boundaries. Since these latter phases arise due to partitioning of Mg, Fe and Si to the inter-dendritic liquid during solidification, they correspond to the last liquid to solidify; as such, the surface grooves correspond to the effect of solidification shrinkage at the cell boundaries that intersect the powder surface. We note that each FCC Al grain consists of one or more cells, with the grain boundaries pinned at the secondary phases. Examples of the STEM data from this prior study are reproduced in Fig. 3.

The microstructure of the heat-treated powders (Figs. 2b and 3b) is not obviously different from that of the as-atomized powders, although it has been shown that there is a subtle reduction in the supersaturation of the Mg in the FCC Al cells [33]. For the homogenized powders, however, there are distinct differences both in the secondary phases and in the grain structure (Figs. 2c and 3c). These correspond to dissolution of the Mg-rich silicides, coarsening of the Fe-rich phase, and unpinning of the grain boundaries leading to grain growth [33,36]. The absence of any concomitant changes in particle surface morphology (Fig. 1d), indicates that the topographic features are established during the initial solidification of the gas-atomized droplets; these features are presumably stabilized by the passivating oxide film since the internal microstructural changes demonstrate that there is significant mass transport occurring at the homogenization temperature.

The characters of the oxide films at the surfaces of the powders were assessed firstly by STEM analyses on FIB-cut cross-sectional specimens,

such as those shown in Fig. 2. An example of a data set obtained from such a specimen of the as-atomized powder is shown in Fig. 4. First, the oxide thickness and cation content were assessed by obtaining line scans from the cross-sections at locations where the metal/oxide and oxide/Pt-cap interfaces are edge-on. Data from one such experiment are shown in Fig. 4a. Spectra were acquired at 0.5 nm intervals along the 50 nm arrow indicated in the HAADF image, which appears as an inset in the upper right corner of the figure. The signal intensities in the O, Mg, Al, Si and Fe K α peak and the Pt L α peak were summed and normalized to show the distributions of the elements. We note that strong scattering from the Pt cap complicates quantification of these data and so only qualitative X-ray data after background subtraction are shown. The oxide film thickness was measured from the trace of the oxygen signal by taking the full width at half maximum to take account of beam broadening within the sample and the effects of the “tails” in the focused beam. Ten such line scans were acquired from the as-atomized specimens, and values of 5.2 ± 0.4 nm were obtained for the oxide thickness. We note that there is a subtle but consistent increase in the Mg and Si signals within the oxide layer in these line scans. Further evidence for this can be seen in X-ray maps from the EDXS spectrum imaging experiments performed on the same area of the cross-section through the particle surface. Fig. 4b-g are normalized maps corresponding to the background-subtracted EDXS signals from O, Al, Mg, Fe, Si and Pt, respectively. The position of the oxide layer is clear from the O map, and there is an obvious enhancement in the Mg and Si

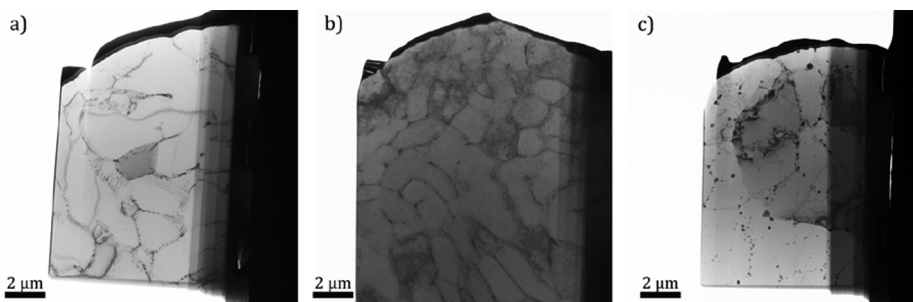


Fig. 2. Low magnification bright field STEM micrographs obtained from FIB-cut cross sections through individual Al 6061 powder particles: a) as-atomized, b) heat-treated, c) homogenized.

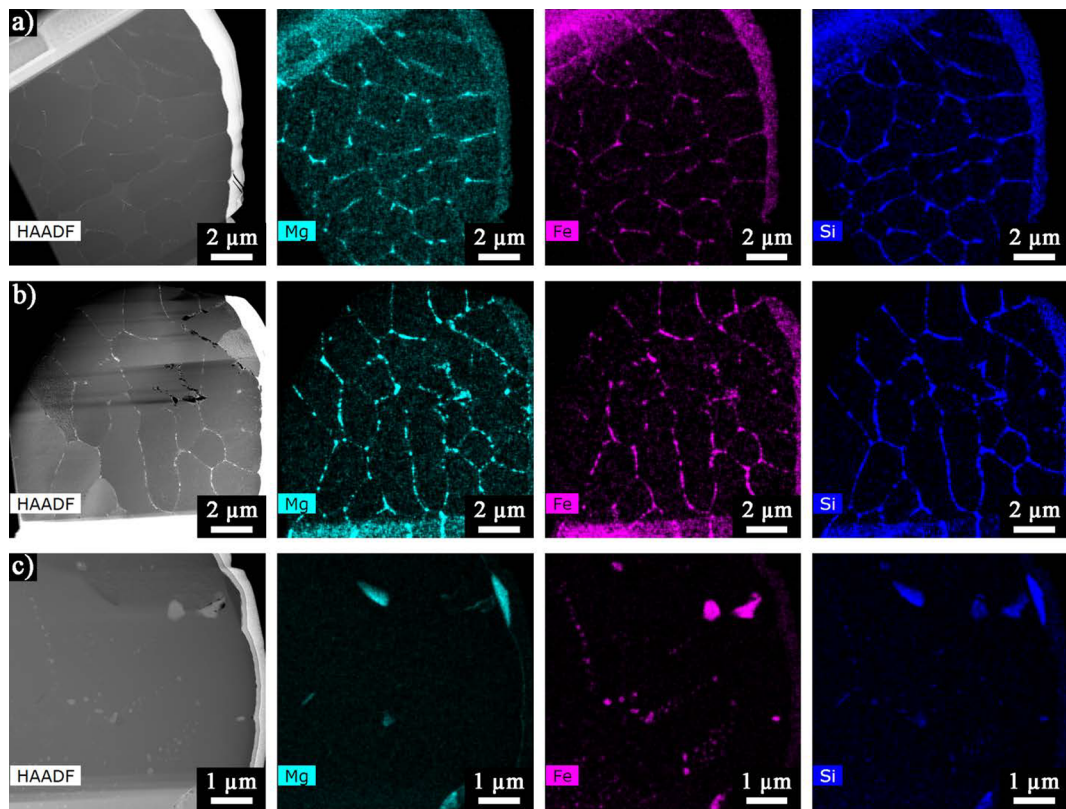


Fig. 3. HAADF STEM images and corresponding EDXS X-ray maps from FIB-cut cross sections through individual powder particles: (a) as-atomized, (b) heat treated, and (c) homogenized. The maps show an increased concentration of Mg, Fe and Si in the cell boundaries of the as-atomized and heat-treated powder particles corresponding to mixtures of silicide phases. There is significant coarsening and partial dissolution of these silicides in the homogenized powder particles. Adapted from [33]

signals in this layer. We note that superposition of these maps suggests that the Mg is concentrated towards the top of the oxide layer, and similar effects can also be observed in the line scan data (Fig. 4a). There is a region at the top of the oxide layer in these maps where there is a reduction in the Al signal, and a significant enhancement in both Mg and Si, both of which appear thicker than the oxide layer at this point. This presumably corresponds to the presence of a magnesium silicide precipitate at the powder particle surface, and indeed this particle was used as a fiducial marker during the line-scan and spectrum imaging experiments. Lastly, we note that the apparent incorporation of Mg, Fe and Si in the Pt layer is an artefact of the data normalization procedure for these minority alloying additions.

Examples of corresponding data sets obtained from cross-sectional specimens of the heat-treated and homogenized powder samples are shown in Figs. 5 and 6, respectively. The data from the heat-treated specimen resemble those from the as-atomized specimen, except that the oxide is a little thicker (6.0 ± 1.0 nm), and the segregation of the Mg towards the top of the oxide layer is more pronounced (Fig. 5a). Here again there are secondary phase particles at the powder particle surface; in this case, there is a coarse triangular magnesium silicide particle at the top of the field of view, and a finer Fe-rich silicide at the bottom (Fig. 5d-f). The data from the homogenized specimen (Fig. 6) exhibit more significant differences. The oxide layer is significantly thicker at 8.9 ± 0.9 nm, and even though the data are not quantified it is clear that the Mg content of the oxide is significantly higher than that for the as-atomized and heat-treated specimens (Fig. 6a). The line scan data also suggest that an oxide bi-layer may be developing with the inner oxide being less Mg-rich than the outer oxide. We note, however that evidence for this is less clear in overlays of the O and Mg maps (Fig. 6b and d) and this may simply correspond to a gradient in the Mg content through the thickness of the oxide layer in the homogenized

specimens.

3.2. X-ray photoelectron spectroscopy

Examples of the XPS data acquired from the as-atomized, heat-treated and homogenized sample powders are presented in Figs. 7, 8 and 9 respectively. Data acquired from the five reference samples under the same experimental conditions are presented in the appendix as Figs. A1–A5 for: T6-Al 6061 sheet; single crystal MgO, MgAl₂O₄ and α -Al₂O₃; and γ -Al₂O₃ powder, respectively. The binding energies obtained from these reference samples were used to identify the different contributions to the XPS peaks measured from the sample powders as described below.

Fig. 7a is a survey spectrum from the as-atomized powder sample; the main XPS peaks are (in order of increasing binding energy): Cl 2 s, C 1s, O 1s and Mg 1s. There are also pronounced Mg KLL and O KLL Auger electron peaks. Weaker XPS peaks were observed at lower binding energies for Mg 2p, Al 2p, Mg 2 s, Al 2 s and Cl 2p, as shown in the inset to Fig. 7a. Information on the chemical environments was obtained by acquiring high-resolution scans from the regions around the Al 2p, O 1s and Mg 1s peaks, as shown in Fig. 7b-d, respectively. Gaussian-Lorentzian deconvolution of the Al 2p peak (Fig. 7b) reveals three distinct contributions centered at binding energies of 74.6, 72.9 and 71.4 eV. These correspond to: Al octahedrally coordinated with O, Al at the metal/oxide interface, and metallic Al, respectively. The octahedrally coordinated Al is the most prominent of these contributions constituting approximately 68% of the Al 2p peak intensity. There are also three contributions to the O 1s peak (Fig. 7c), although in this case the symmetry of the peak gives greater uncertainty in the exact positions and weightings of these contributions. These occur at binding energies of 531.7, 530.9 and 530.2 eV, corresponding to: O bound in a non-

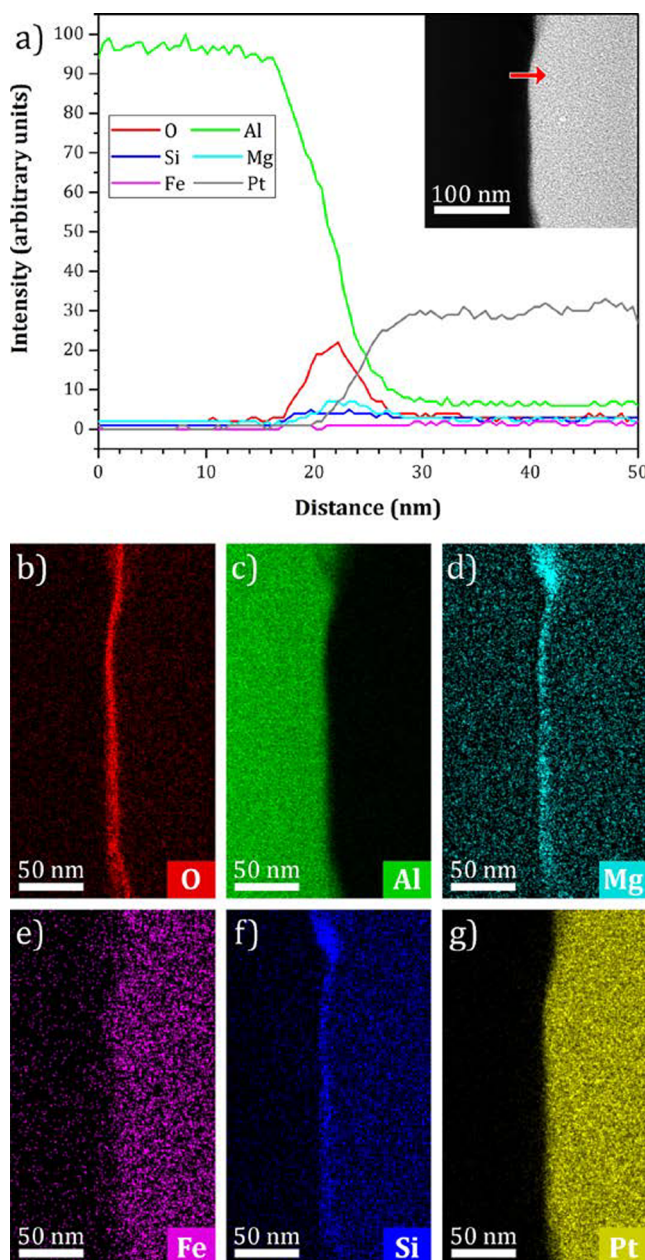


Fig. 4. STEM-EDXS data collected from a FIB-cut cross section through the surface of an as-atomized powder particle: a) line scan data taken from the position indicated by the red arrow in the inset HAADF image; b)-g) X-ray maps extracted from a spectrum imaging experiment on the region of the surface shown in the HAADF image in a) above.

stoichiometric alumina environment, O bound to octahedrally coordinated Al, and O bound to Mg. The Mg 1s signal consists of a single Gaussian peak at 1304.5 eV. This is consistent with Mg bound to O, but no further information can be deduced about the coordination since the binding energies of octahedrally- and tetrahedrally-coordinated Mg (as in rock-salt MgO and the normal spinel $MgAl_2O_4$, respectively) are almost identical.

The corresponding plots from the heat-treated powder sample are presented in Fig. 8. The Al 2p peak (Fig. 8b) has a larger contribution from octahedrally-coordinated Al-O (at 74.6 eV), a smaller contribution from interfacial Al-O (at 72.3 eV) and no metallic Al, presumably because of the thickening of the oxide layer. The O 1s peak (Fig. 8c) includes contributions from adsorbed surface O (at 532.5 eV) and lattice oxygen (at 531.4 eV) the appearance of the latter contribution is

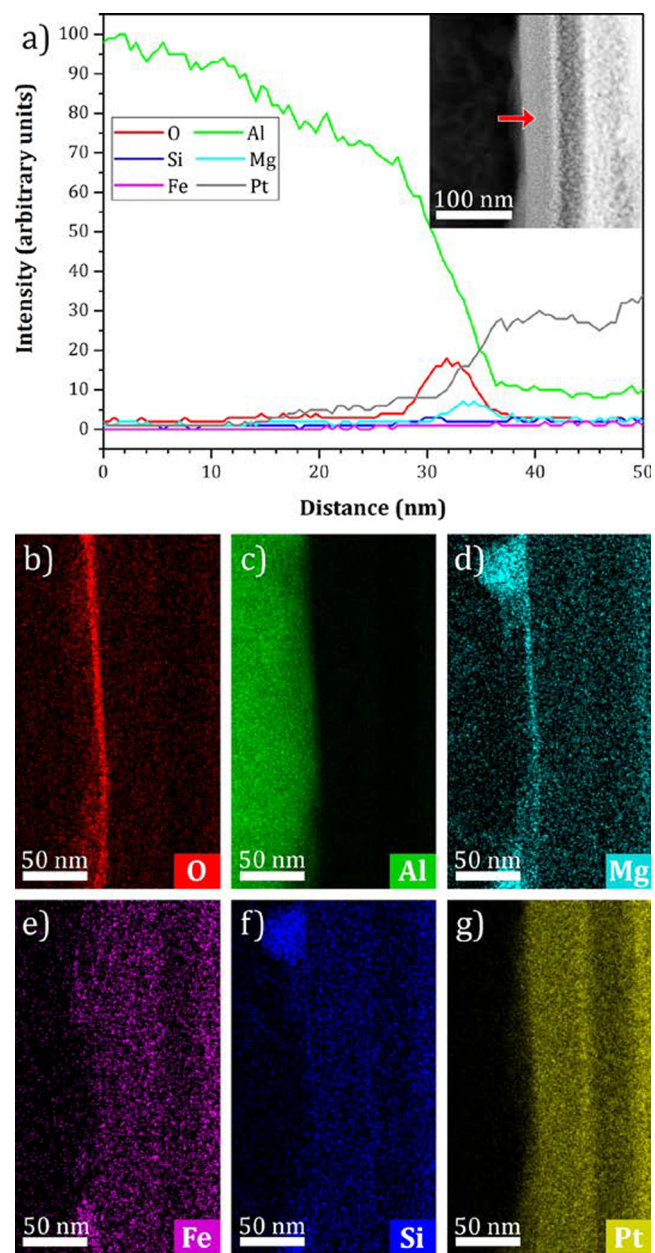


Fig. 5. STEM-EDXS data collected from a FIB-cut cross section through the surface of a heat-treated powder particle: a) line scan data taken from the position indicated by the red arrow in the inset HAADF image; b)-g) X-ray maps extracted from a spectrum imaging experiment on the region of the surface shown in the HAADF image in a) above.

consistent with the crystallization of the oxide during the heat-treatment process. The plots from the homogenized powder sample are presented in Fig. 9. The Al 2p peak (Fig. 9b) shows distinct changes with roughly equal contributions from octahedrally- and tetrahedrally-coordinated Al-O (at 74.4 and 73.6 eV, respectively), with no contribution from interfacial Al-O or metallic Al; this is consistent with both further thickening of the oxide layer and a structural transformation. The O 1s peak (Fig. 9c) also suggests structural changes with contributions from adsorbed O, edge-bound surface O and lattice O (at 532.5, 531.8 and 531.3 eV, respectively).

The energies and percentage contributions for the Al 2p, O 1s and Mg 1s peaks from each of the three samples are presented in Table 1 together with the values from the five reference samples for comparison.

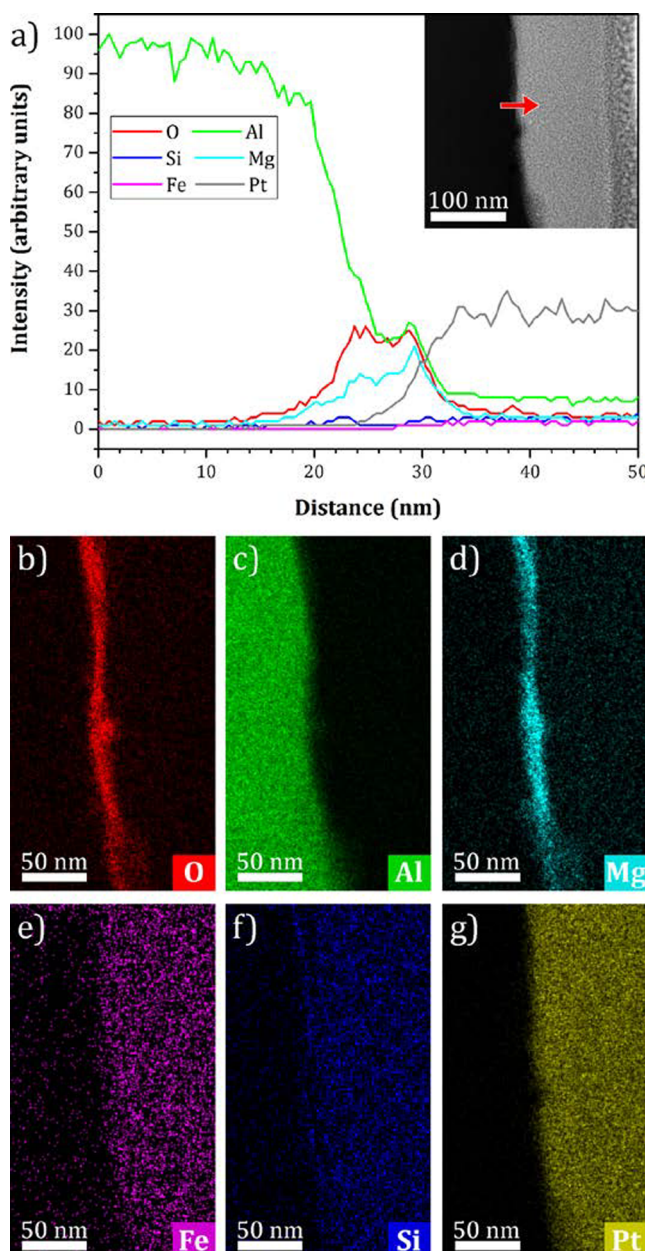


Fig. 6. STEM-EDXS data collected from a FIB-cut cross section through the surface of a homogenized powder particle: a) line scan data taken from the position indicated by the red arrow in the inset HAADF image; b)-g) X-ray maps extracted from a spectrum imaging experiment on the region of the surface shown in the HAADF image in a) above.

4. Discussion

The objective of this study was to investigate the effects of typical thermal treatments used for Al 6061 CGDS feedstocks on the surface oxide layers formed on the gas atomized powder particles. The internal microstructures of these powders have been discussed in detail elsewhere [33], and the STEM data obtained from the particle interiors in FIB-cut cross sections (Figs. 2 and 3) are all consistent with results of that prior study. The overall morphologies of the powder particles are not affected by the heat treatments (Fig. 1) and only in the cross-sectional STEM data (Figs. 4-6) and the XPS data (Figs. 7-9) are significant differences observed between the samples. The most significant effect is the enhancement of the Mg content at the surface as compared to that in the underlying FCC Al matrix. While the alloy Al 6061 contains around 1% Mg overall, a significant proportion of this is in the form of Mg₂Si phases distributed throughout the

microstructure, and the maximum Mg content measured in the matrix is around 0.7 at.% [33]. As explained in section 3.1, the line scan data cannot be quantified accurately due to the scattering in the Pt cap, but the Mg content is clearly much higher at the surface, particularly in the case of the homogenized powder.

The formation of Mg-rich surface oxides on binary Al-Mg alloys, and in Al-Mg-Si alloys such as Al 6061, has been reported in detail in the literature (e.g. [37–47]). The character and formation mechanism for the oxide scales varies somewhat with the alloy chemistry, the oxidation temperature, and the oxygen partial pressure, but nonetheless there are certain common trends. At low temperatures and oxygen partial pressures an amorphous aluminum oxide layer forms on the alloys. As for pure Al, this amorphous layer reaches a limiting thickness due to the kinetics of mass transport for Al to the oxide surface and/or O to the oxide/metal interface. At higher temperatures, the amorphous oxide crystallizes to form γ -Al₂O₃ at the oxide/metal interface, and there is outward diffusion of Mg, which is oxidized selectively at the free surface. The Mg-rich oxidation products are crystalline, with spinel MgAl₂O₄ being favored for more dilute alloys, and rock-salt MgO forming on more concentrated Al-Mg alloys, although in many cases a mixture or layers of MgAl₂O₄ and MgO develop.

The situation considered here is rather different. The thin oxide scales on the as-atomized powder particles show significant enhancement in Mg, even though these were formed by allowing the pristine powder to cool thoroughly before bleeding oxygen into the apparatus to prevent spontaneous ignition. Moreover, both the Mg-rich surface oxide sub-layer and the underlying Mg-lean oxide sub-layer appear to be amorphous with no obvious contribution from lattice oxygen in the O 1s XPS peak. This is consistent with the segregation of the Mg to the surface during solidification, rather than during the introduction of oxygen. Such an effect would also explain why amorphous Mg-rich and Mg-lean sub-layers are formed during the introduction of oxygen at low temperatures, rather than the crystalline MgAl₂O₄ and MgO that form when Mg migrates to the surface at high temperatures under the driving force of selective oxidation. Segregation to the powder particle surface during solidification can be understood if one considers that there is significant undercooling of the gas-atomized droplets during powder production. The onset of solidification occurs by the nucleation of the FCC Al matrix phase at exogenous heterogeneous nucleants within each droplet [33]. Partitioning of the alloying elements to the liquid phase at the solidification front leads to the cellular-dendritic solidification microstructure observed experimentally (Fig. 2a), with segregation to the cell boundaries and to the droplet surface.

It is important to note that the oxide layers observed on the heat-treated and the homogenized powders result from two different thermal processing routes, both of which start with the same as-atomized powder.

The heat-treated powder was held at 230 °C for 75 min. Under these conditions one would expect no thickening or crystallization of the surface oxide on pure Al [48,49]. In the STEM data (such as Fig. 5) obtained from FIB-cut cross-sections through the surfaces of the heat-treated powders, two distinct changes were observed in the oxide: a small but significant thickening from 5.2 to 6.0 nm, and the development of a more clearly defined Mg-rich outer layer and Mg-lean inner layer. This is accompanied by a strong contribution from lattice oxygen in the O 1s XPS peak, corresponding to crystallization. We note that the heat-treatment temperature is well below that at which pure aluminum oxide crystallizes to γ -Al₂O₃, and that there is no contribution from the tetrahedrally-coordinated Al-O in the Al 2p XPS peak that one would expect for the γ spinel polymorph of alumina. The crystallization is instead consistent with the formation of an outer layer of normal spinel MgAl₂O₄, in which the Mg and Al cations are tetrahedrally and octahedrally coordinated, respectively (e.g. [50]). Since the Mg content in the oxide appears to be qualitatively similar to that in oxide for the as-atomized powder, this process could simply represent local redistribution and rearrangement of the cations with the oxide layer, and the Mg-lean inner aluminum oxide layer is presumably still amorphous for powders in this condition.

The homogenized powder was subjected to a more complex thermal sequence that involved holding at 400 °C for 2 h, and at 530 °C 30 min, all

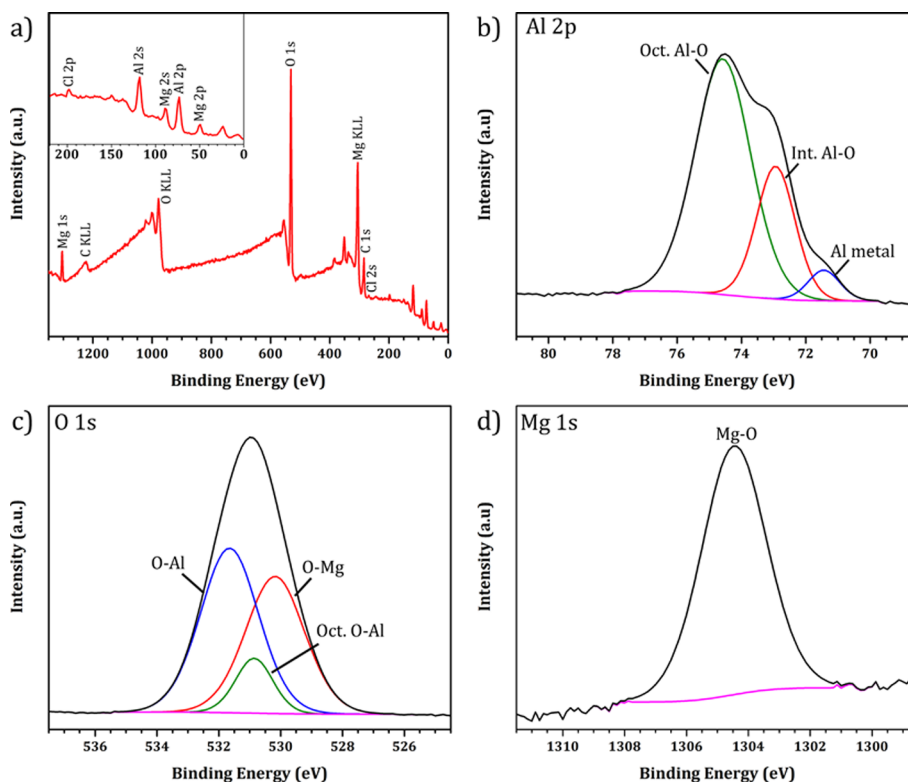


Fig. 7. XPS spectra collected from a sample of atomized powder particles: a) survey scan. b-d) high resolution scans of Al 2p, O 1s, and Mg 1s peaks, respectively. The Al 2p peak includes contributions from aluminum octahedrally coordinated with oxygen (Oct. Al-O), from aluminum at the metal/oxide interface (Int. Al-O), and from the underlying aluminum metal. The O 1s peak includes components from oxygen bound to under-coordinated aluminum (O-Al), from oxygen bound to octahedrally-coordinated aluminum (Oct. O-Al), and from oxygen bound to Mg (O-Mg).

under Ar in a sealed retort to prevent excessive oxidation. Thus, the powder experienced a low (if rather ill-defined) partial pressure of oxygen during the thermal exposure. The cross-sectional STEM data from such powders (Fig. 6) show a more distinct thickening of the oxide to 8.9 nm and the development of a double layer in which the outer layer is Mg-rich, but the inner layer also contains significant amounts of

Mg, and there is no Mg-lean (i.e. essentially pure) aluminum oxide layer. Here again, there is a strong contribution from lattice oxygen in the O 1s XPS peak, but in this case the peak temperature is well above that at which aluminum oxide crystallizes, and there are strong contributions from both tetrahedrally- and octahedrally-coordinated Al-O in the Al 2p XPS peak. Since there is no pure aluminum oxide layer, this

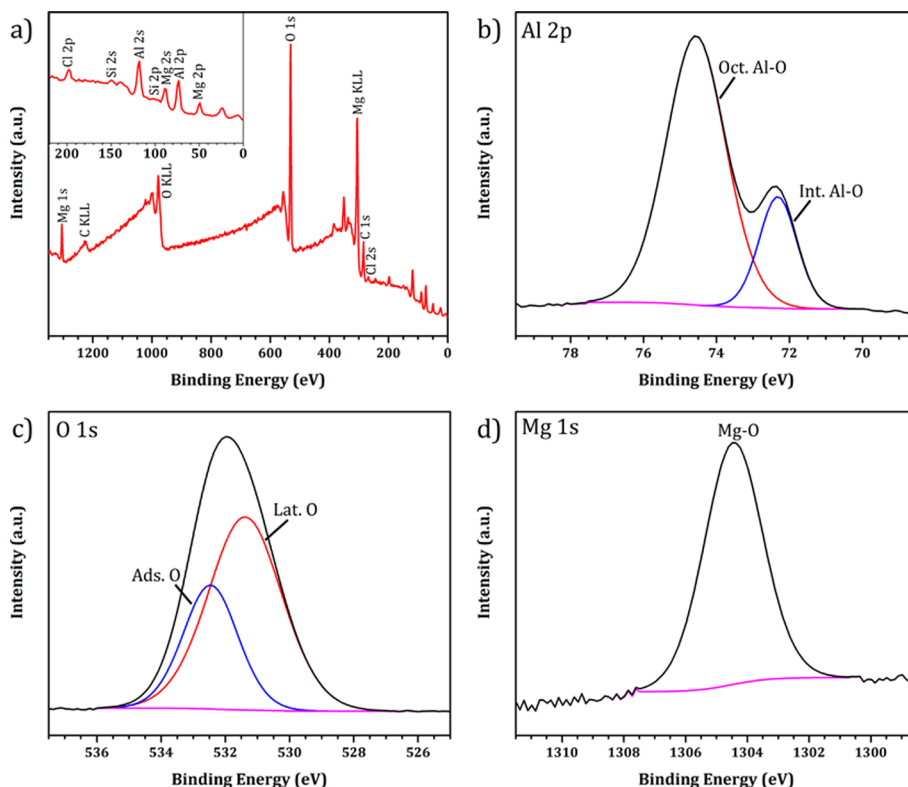


Fig. 8. XPS spectra collected from a sample of heat-treated powder particles: a) survey scan. b-d) high resolution scans of Al 2p, O 1s, and Mg 1s peaks, respectively. The Al 2p peak includes contributions from aluminum octahedrally coordinated with oxygen (Oct. Al-O), and from aluminum at the metal/oxide interface (Int. Al-O). The O 1s peak includes components from adsorbed surface oxygen (Ads. O) and from lattice oxygen (Lat. O).

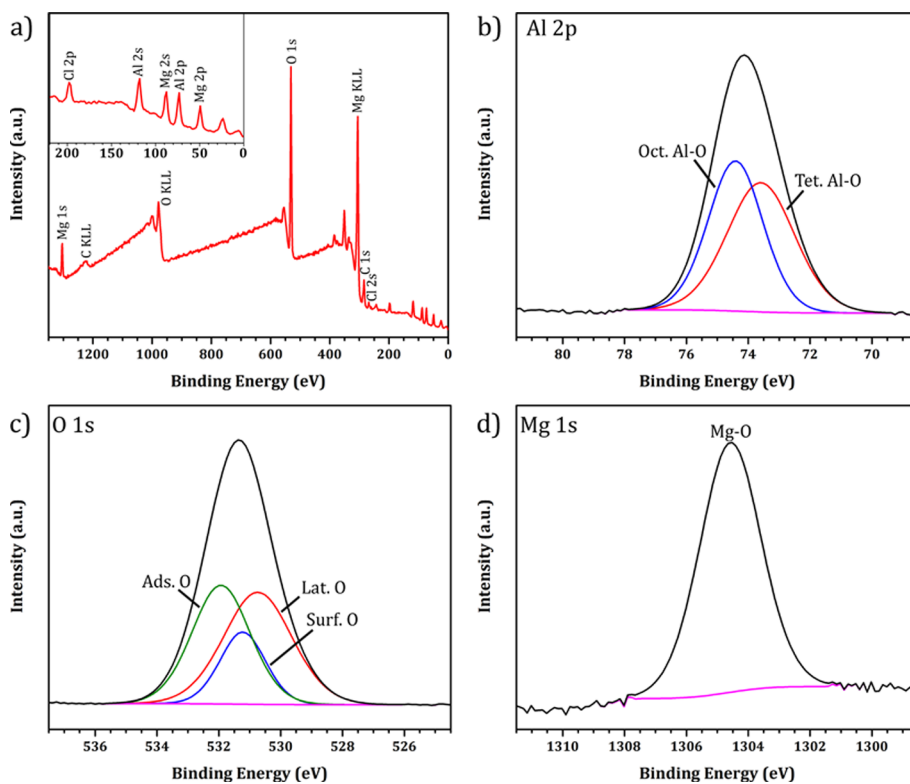


Fig. 9. XPS spectra collected from a sample of homogenized powder particles: a) survey scan. b-d) high resolution scans of Al 2p, O 1s, and Mg 1s peaks, respectively. The Al 2p peak includes contributions from aluminum octahedrally and tetrahedrally coordinated with oxygen (Oct. Al-O and Tet. Al-O, respectively). The O 1s peak includes components from adsorbed surface oxygen (Ads. O), from surface bound oxygen (Surf. O) and from lattice oxygen (Lat. O).

cannot simply be due to a $\gamma\text{-Al}_2\text{O}_3$ inner layer being formed between the alloy and the MgAl_2O_4 spinel outer layer. Instead, we infer that the tetrahedrally-coordinated Al-O corresponds to an inverse spinel Al ($\text{Mg},\text{Al})_2\text{O}_4$ that forms as the amorphous alumina crystallizes under the influence of a flux of Mg from the underlying alloy. In such an inverse spinel, Al^{3+} would occupy both the tetrahedral sites and some of the octahedral sites, while Mg^{2+} occupies the remainder of the octahedral sites. For charge balance, one would expect equal numbers of Al^{3+} and Mg^{2+} if the spinel were stoichiometric, but since $\gamma\text{-Al}_2\text{O}_3$ is itself a defect spinel, a range of compositions between pure alumina and the stoichiometric spinel are possible. Indeed, the STEM EDXS data in Fig. 6 do indicate that the inner oxide layer is leaner in Mg than the outer MgAl_2O_4 spinel oxide layer.

While the findings reported here are somewhat different from those in the literature on oxidation of Al-Mg-based alloys, we note that such studies are usually performed on planar sections cut from the alloys. This is, in part, for experimental convenience since the quantification of spectrometric data is much more reliable when performed on flat sample surfaces. Moreover, flat samples allow for techniques such as glancing incidence X-ray diffraction to be used to identify thin crystalline phases. The drawback with such studies is that they give

information on the oxidation behavior of the *interior* of the material and cannot capture effects such as the surface segregation that occurs during solidification of gas-atomized powders. It is known that the oxides formed on such powders can have a profound influence on the sintering behavior for more conventional powder metallurgy processing (e.g. [51–54]), but only recently have these issues been considered in detail for GDCS of Al alloy powders (e.g. [30,55]). Clearly, the differences in the surface oxides observed in this study could result in rather different critical velocities and bonding characteristics when these powders are used as GDCS feedstocks. Moreover, the specimen preparation and analysis approaches adopted here are not designed to preserve the hydration state of the surface oxides, which could also affect the bonding during GDCS, particularly for amorphous surface layers. Further work is underway to investigate these effects.

5. Conclusions

A combination of cross-sectional STEM and XPS studies have been used to examine Al 6061 gas atomized powders in the as-atomized state and after two different thermal exposures that correspond to typical pre-treatment conditions for GDCS of Al 6061. The main findings are as

Table 1

Binding energies for XPS peaks (including contributions from deconvoluted peaks where appropriate) from as-atomized, heat-treated and homogenized powder samples (Figs. 6–8, respectively) and from standards of: wrought Al 6061 sheet; single crystal substrates of MgO , MgAl_2O_4 and $\alpha\text{-Al}_2\text{O}_3$; and $\gamma\text{-Al}_2\text{O}_3$ powder (Figs. A1–A5, respectively).

Region	Peak binding energy position(s) (eV) (at%)							
	As Atomized	Heat Treated	Homogenized	Al6061	MgO	MgAl_2O_4	$\alpha\text{-Al}_2\text{O}_3$	$\gamma\text{-Al}_2\text{O}_3$
Al 2p	74.6 (68%)	74.6 (79%)	74.4 (52%)	75.1 (89%)	N/A	74.5	74.1	74.5 (55%)
	72.9 (27%)	72.3 (21%)	73.6 (48%)	73.0 (11%)				73.7 (45%)
	71.4 (5%)							
O 1s	531.7 (49%)	532.5 (68%)	532.5 (39%)	532.3 (50%)	532.4 (16%)	531.2	530.8	532.6 (41%)
	530.9 (10%)	531.4 (32%)	531.8 (18%)	531.2 (50%)	530.0 (84%)			531.7 (13%)
	530.2 (41%)		531.3 (43%)					531.0 (46%)
Mg 1s	1304.5	1304.5	1304.6	1304.5	1304.2	1304.3	N/A	N/A

follows:

1. The as-atomized powders have amorphous surface oxide layers ≈ 5.2 nm in thickness comprising an outer Mg-rich sub-layer and an inner Mg-lean aluminum oxide sub-layer.
2. Powders heat-treated in air at 230 °C have slightly thicker surface oxide layers (≈ 6.0 nm) with a crystalline MgAl_2O_4 spinel outer sub-layer and an amorphous aluminum oxide inner sub-layer.
3. Powders heat-treated under Ar at 400 and 530 °C have significantly thicker surface oxide layers (≈ 8.9 nm) with an MgAl_2O_4 spinel outer sub-layer and a defect inverse spinel $\text{Al}(\text{Mg},\text{Al})_2\text{O}_4$ inner layer.

The differences between these observations and previous reports on oxidation of planar sections cut from similar alloys can be explained on the basis of surface segregation of Mg during the cellular dendritic solidification of the droplets formed during gas atomization. This gives amorphous layers during initial stabilization of the as-atomized powder, crystallization of the outer sub-layer by local atomic rearrangement during low-temperature heat-treatment in air, and the formation and growth of spinel sub-layers due to outward diffusion of Mg during high-temperature heat-treatment under Ar.

Data availability

The raw/processed data required to reproduce these findings cannot be shared at this time as the data also form part of an ongoing study.

Appendix A. XPS data from standard samples

To assist in the identification of the deconvoluted components of the Al 2p and O 1s XPS peaks from the oxides on the Al 6061 powder samples, spectra were obtained from standard samples under the same instrumental conditions. The standards were: polycrystalline Al 6061 sheet in the T6 condition; single crystal substrates of MgO (rocksalt structure), MgAl_2O_4 (spinel) and $\alpha\text{-Al}_2\text{O}_3$ (sapphire); and $\gamma\text{-Al}_2\text{O}_3$ powders. The XPS spectra from these standards are included here as Figs. A1-A5, respectively. The binding energies for the peaks, or the deconvoluted contributions as appropriate, are included in Table 1 in the main text.

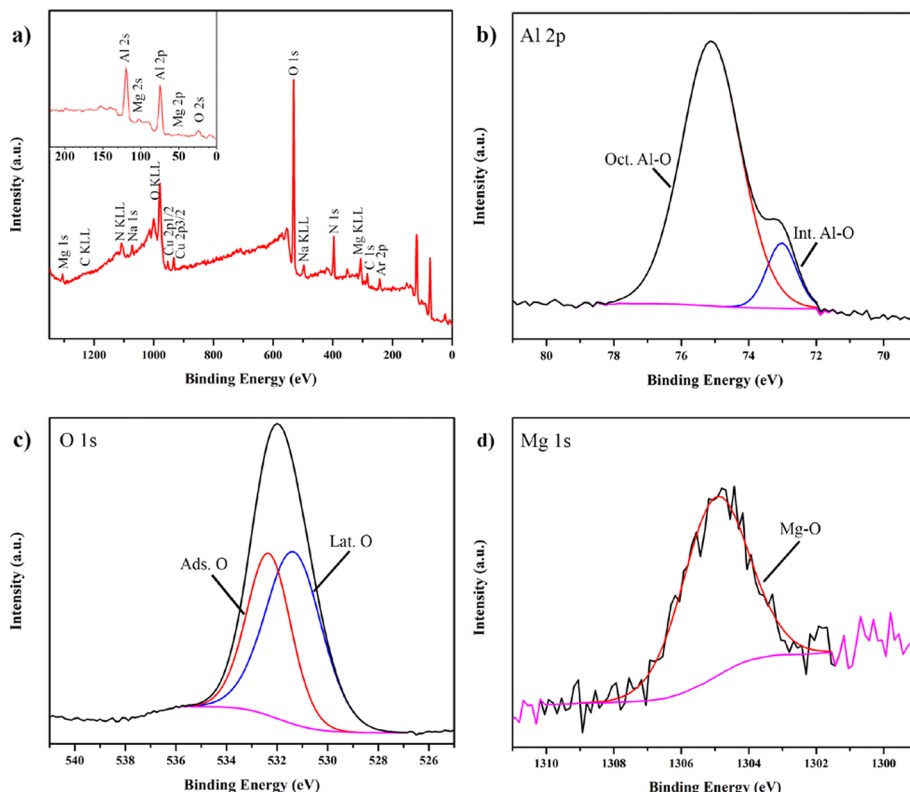


Fig. A1. XPS spectra collected from the Al6061-T6 standard: a) survey scan. b-d) high resolution scans of Al 2p, O 1s, and Mg 1s, respectively. The Al 2p peak includes contributions from aluminum octahedrally coordinated with oxygen (Oct. Al-O), and from aluminum at the metal/oxide interface (Int. Al-O). The O 1s peak includes components from adsorbed surface oxygen (Ads. O) and from lattice oxygen (Lat. O). The Mg 1s peak is very weak and “noisy” due to the low magnesium content in the surface oxide.

CRediT authorship contribution statement

Alexis T. Ernst: Investigation, Formal analysis, Writing - original draft, Visualization. **Peter Kerns:** Investigation, Formal analysis, Visualization. **Aaron Nardi:** Investigation, Methodology, Project administration. **Harold D. Brody:** Supervision. **Avinash M. Dongare:** Supervision. **Seok-Woo Lee:** Supervision. **Victor K. Champagne:** Funding acquisition, Project administration. **Steven L. Suib:** Supervision, Writing - review & editing. **Mark Aindow:** Conceptualization, Writing - review & editing, Supervision, Project administration, Funding acquisition.

Declaration of Competing Interest

The authors declare that they have no known competing financial interests or personal relationships that could have appeared to influence the work reported in this paper.

Acknowledgements

This research was supported by the U.S. Army Research Laboratory under contract W911NF-15-2-0024, titled “Intelligent Processing of Materials by Design”. The microscopy studies in this paper were performed using the facilities in the UConn/Thermo Fisher Scientific Center for Advanced Microscopy and Materials Analysis (CAMMA).

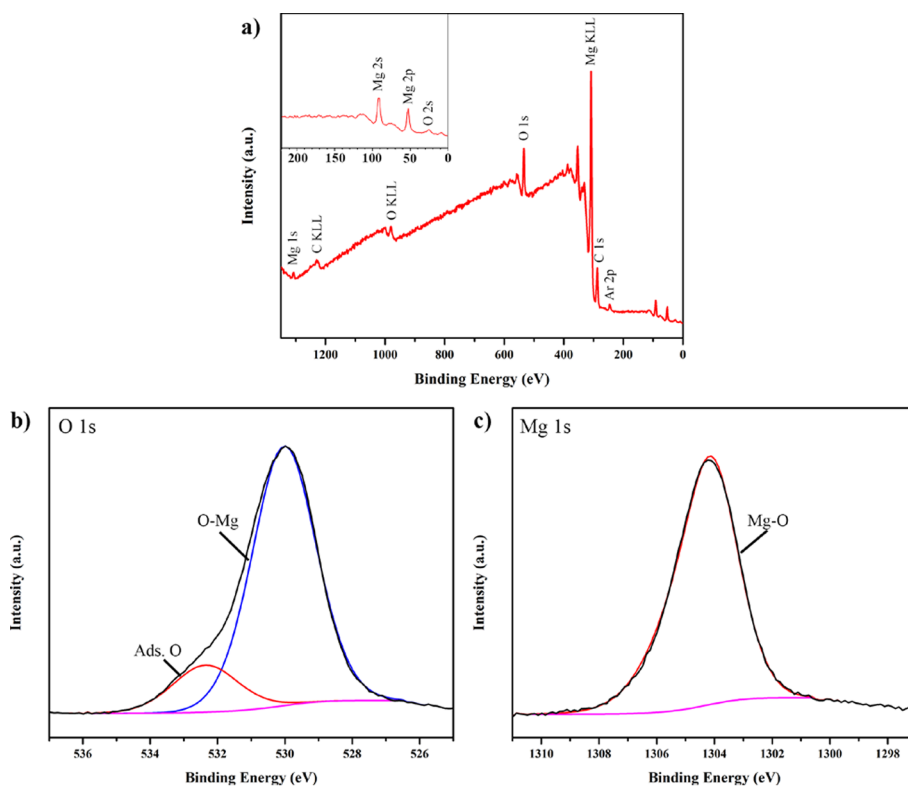


Fig. A2. XPS spectra collected from the MgO standard: a) survey scan; b)-c) high resolution scans of O 1s, and Mg 1s, respectively. The O 1s peak includes components from adsorbed surface oxygen (Ads. O) and from oxygen bound to Mg (O-Mg).

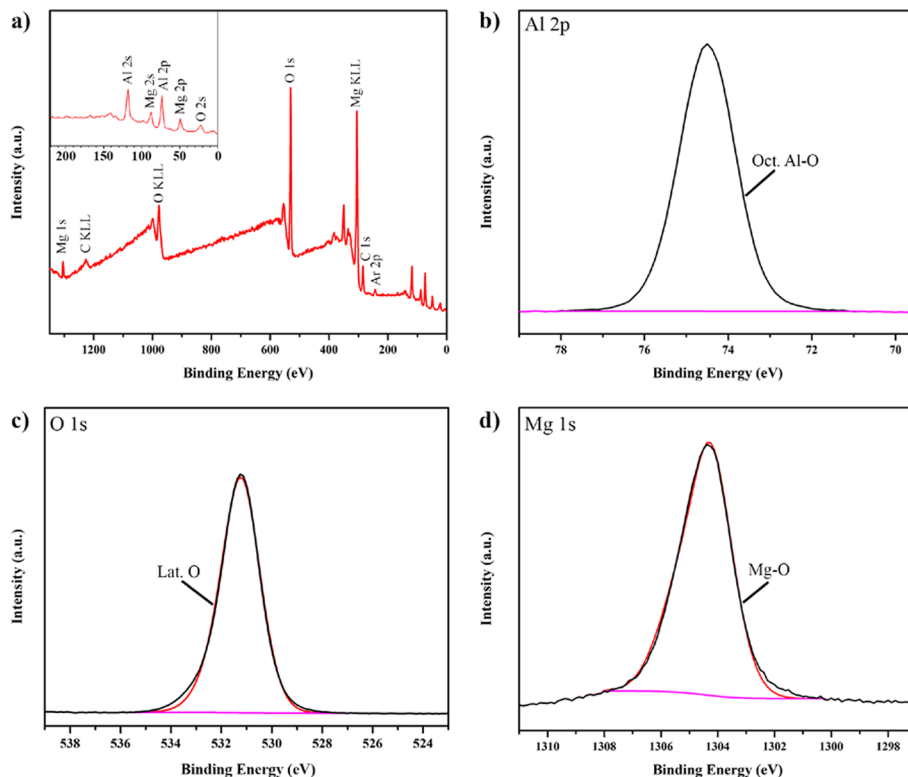


Fig. A3. XPS spectra collected from the MgAl₂O₄ standard: a) survey scan; b)-d) high resolution scans of Al 2p, O 1s, and Mg 1s, respectively. The Al 2p peak corresponds to aluminum octahedrally coordinated with oxygen (Oct. Al-O), while the O 1s corresponds to lattice oxygen (Lat. O).

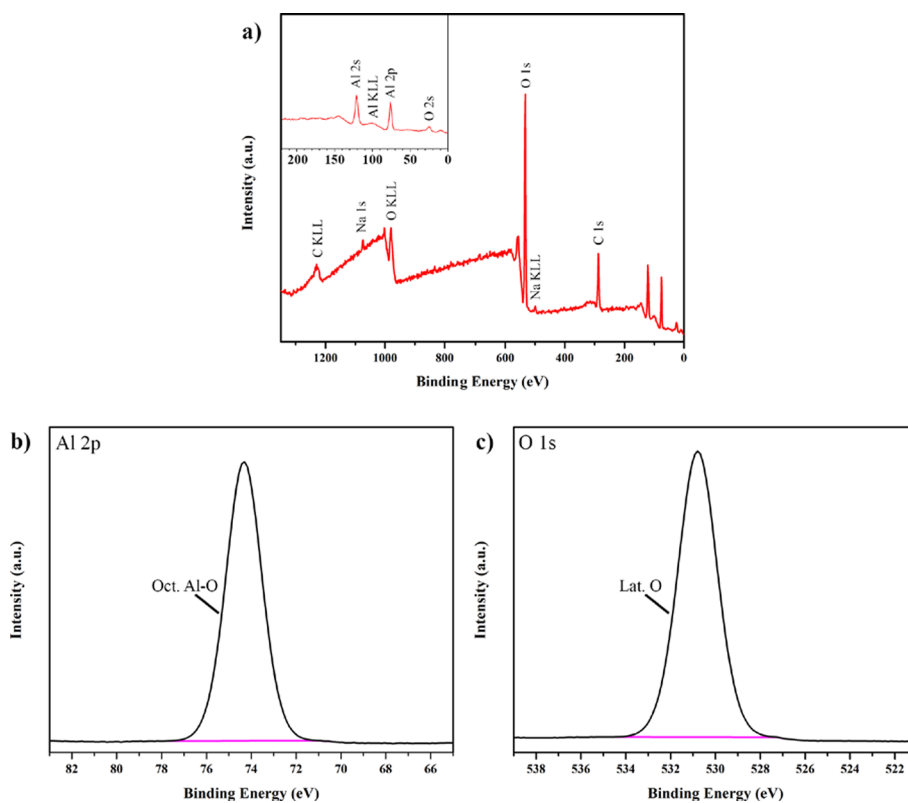


Fig. A4. XPS spectra collected from the α -Al₂O₃ standard: a) survey scan; b)-c) high resolution scans of Al 2p and O 1s, respectively. The Al 2p peak corresponds to aluminum octahedrally coordinated with oxygen (Oct. Al-O), while the O 1s corresponds to lattice oxygen (Lat. O).

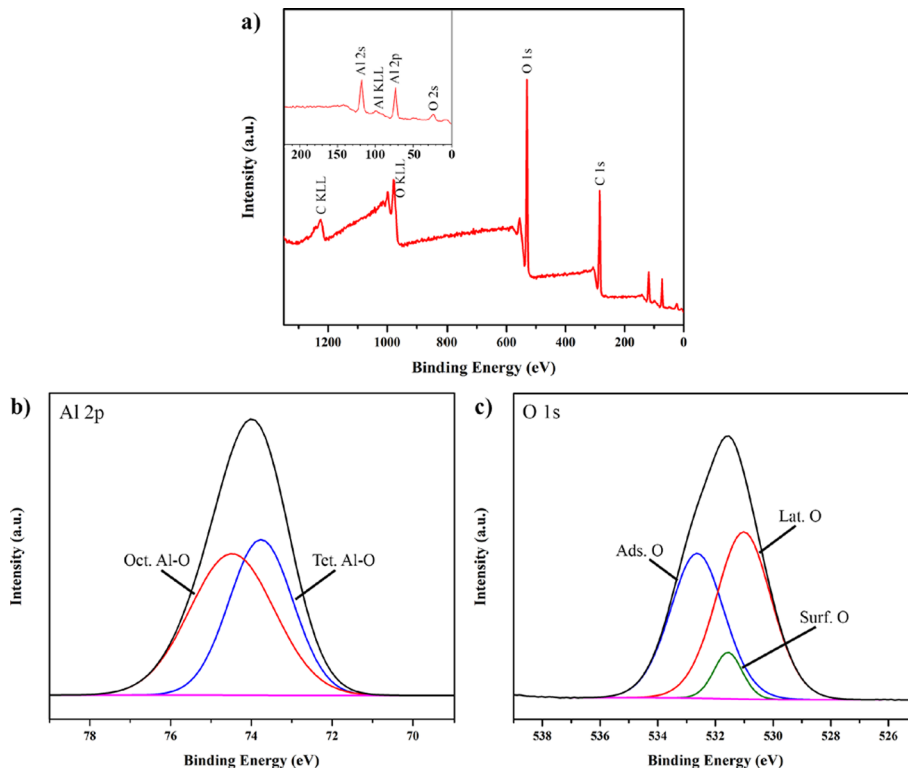


Fig. A5. XPS spectra collected from the γ -Al₂O₃ standard: a) survey scan; b)-c) high resolution scans of Al 2p and O 1s, respectively. The Al 2p peak includes contributions from aluminum octahedrally and tetrahedrally coordinated with oxygen (Oct. Al-O and Tet. Al-O, respectively), as expected for the defect spinel structure. The O 1s peak includes components from adsorbed surface oxygen (Ads. O), from surface bound oxygen (Surf. O) and from lattice oxygen (Lat. O); the former contributions arise because the γ -Al₂O₃ is in the form of nanoscale plate-like particles.

References

- [1] R.M. German, Powder Metallurgy Science, second ed., Metal Powder Industries Federation, Princeton, New Jersey, U.S.A, 1994.
- [2] W.E. Frazier, Metal additive manufacturing: a review, J. Mater. Eng. Perform. 23 (2014) 1917–1928.
- [3] D. Herzog, V. Seyda, E. Wycisk, C. Emmelmann, Additive manufacturing of metals, Acta Mater. 117 (2016) 371–392.
- [4] E.J. Lavernia, Evolution of microstructure during spray atomization and deposition, Int. J. Rapid Solid. 5 (1989) 47–85.
- [5] H. Karlsson, L. Nyborg, S. Berg, Surface chemical analysis of prealloyed water

- atomised steel powder, *Powder Metall.* 48 (2005) 51–58.
- [6] D. Chasoglou, E. Hryha, M. Norell, L. Nyborg, Characterization of surface oxides on water-atomized steel powder by XPS/AES depth profiling and nano-scale lateral surface analysis, *Appl. Surf. Sci.* 268 (2013) 496–506.
- [7] H. Danninger, C. Gierl, Processes in PM steel compacts during the initial stages of sintering, *Mater. Chem. Phys.* 67 (2001) 49–55.
- [8] E. Hryha, C. Gierl, L. Nyborg, H. Danninger, E. Dudrova, Surface composition of the steel powders pre-alloyed with manganese, *Appl. Surf. Sci.* 256 (2010) 3946–3961.
- [9] R.J. Hebert, Viewpoint: metallurgical aspects of powder bed metal additive manufacturing, *J. Mater. Sci.* 51 (2016) 1165–1175.
- [10] C.L.A. Leung, S. Marussi, M. Towrie, R.C. Atwood, P.J. Withers, P.D. Lee, The effect of powder oxidation on defect formation in laser additive manufacturing, *Acta Mater.* 166 (2019) 294–305.
- [11] S. Özbilgen, A. Ünal, T. Sheppard, Influence of atomizing gases on the oxide-film morphology and thickness of aluminum powders, *Oxid. Met.* 63 (2000) 1–23.
- [12] H. Jones, Gas-atomised aluminium alloy powders and their products: An update 1996–2001, *Mater. Sci. Eng. A* 375–377 (2004) 104–111.
- [13] D.S. Sundaram, P. Puri, V. Yang, A general theory of ignition and combustion of nano- and micron-sized aluminum particles, *Combust. Flame* 169 (2016) 94–109.
- [14] A. Nylund, I. Olefjord, Surface analysis of air exposed rapidly solidified aluminum powder, *Powder Metall.* 36 (1993) 193–197.
- [15] M.K. Miller, Determining the role of surfaces and interfaces in the powder metallurgy processing of aluminum alloy powders, *Surf. Interf. Anal.* 31 (2001) 599–608.
- [16] J.F. Flumerfelt, Aluminum powder metallurgy processing, PhD dissertation Iowa State University, 1998.
- [17] F. Tang, I.E. Anderson, S.B. Biner, Solid state sintering and consolidation of Al powders and Al matrix composites, *J. Light. Met.* 2 (2002) 201–214.
- [18] T.H. Van Steenkiste, J.R. Smith, R.E. Teets, J.J. Moleski, D.W. Gorkiewicz, R.P. Tison, D.R. Marantz, K.A. Kowalsky, W.L. Riggs II, P.H. Zajchowski, B. Pilsner, R.C. McCune, K.J. Barnett, Kinetic Spray Coatings, *Surf. Coat. Technol.* 111 (1999) 62–71.
- [19] V.K. Champagne (Ed.), The Cold Spray Materials Deposition Process: Fundamentals and Applications, Woodhead Publishing Limited, Abingdon Hall, 2007.
- [20] A. Moridi, S.M. Hassani-Gangaraj, M. Guagliano, M. Dao, Cold spray coating: review of material systems and future perspectives, *Surf. Eng.* 30 (2014) 369–395.
- [21] R.C. Dykhuizenn, M.F. Smith, D.L. Gilmore, R.A. Neiser, X. Jiang, S. Sampath, Impact of high velocity cold spray particles, *J. Therm. Spray Tech.* 8 (1999) 559–564.
- [22] D.L. Gilmore, R.C. Dykhuizenn, R.A. Neiser, T.J. Roemer, M.F. Smith, Particle velocity and deposition efficiency in the cold spray process, *J. Therm. Spray Tech.* 8 (1999) 576–582.
- [23] M.R. Rokni, S.R. Nutt, C.A. Widener, V.K. Champagne, R.H. Hrabe, Review of relationship between particle deformation, coating microstructure, and properties in high-pressure cold spray, *J. Therm. Spray Tech.* 26 (2017) 1308–1355.
- [24] H. Assadi, F. Gärtner, T. Stoltzenhoff, H. Kreye, Bonding mechanism in cold gas spraying, *Acta Mater.* 51 (2003) 4379–4394.
- [25] W.-Y. Li, C.-J. Li, H. Liao, Significant influence of particle surface oxidation on deposition efficiency, interface microstructure and adhesive strength of cold-sprayed copper coatings, *Appl. Surf. Sci.* 256 (2010) 4953–4958.
- [26] S. Yin, X. Wang, W. Li, H. Liao, H. Jie, Deformation behavior of the oxide film on the surface of cold sprayed powder particle, *Appl. Surf. Sci.* 259 (2012) 294–300.
- [27] K. Kim, W. Li, X. Guo, Detection of oxygen at the interface and its effect on strain, stress, and temperature at the interface between cold sprayed aluminum and steel substrate, *Appl. Surf. Sci.* 357 (2015) 1720–1726.
- [28] M. Hassani-Gangaraj, D. Veysset, V.K. Champagne, K.A. Nelson, C.A. Schuh, Adiabatic shear instability is not necessary for adhesion in cold spray, *Acta Mater.* 158 (2018) 430–439.
- [29] S. Suresh, S.-W. Lee, M. Aindow, H.D. Brody, V.K. Champagne, A.M. Dongare, Unraveling the mesoscale evolution of microstructure during supersonic impact of aluminum powder particles, *Sci. Rep.* 8 (2018) 10075.
- [30] M. Hassani-Gangaraj, D. Veysset, K.A. Nelson, C.A. Schuh, Impact-bonding with aluminum, silver, and gold microparticles: Toward understanding the role of native oxide layer, *Appl. Surf. Sci.* 476 (2019) 528–532.
- [31] A. Viscusi, A. Astarita, R. Della Gatta, F. Rubino, A perspective review on the bonding mechanisms in cold gas dynamic spray, *Surf. Eng.* 35 (2019) 743–771.
- [32] S. Suresh, S.-W. Lee, M. Aindow, H.D. Brody, V.K. Champagne, A.M. Dongare, Mesoscale modeling of jet initiation behavior and microstructural evolution during cold spray single particle impact, *Acta Mater.* 182 (2020) 197–206.
- [33] B.A. Bedard, T.J. Flanagan, A.T. Ernst, A. Nardi, A.M. Dongare, H.D. Brody, V.K. Champagne Jr., S.-W. Lee, M. Aindow, Microstructure and micromechanical response in gas-atomized Al 6061 alloy powder and cold-sprayed splats, *J. Therm. Spray Tech.* 27 (2018) 1563–1578.
- [34] T.J. Flanagan, B.A. Bedard, A.V. Dongare, H.D. Brody, A. Nardi, V.K. Champagne Jr., M. Aindow, S.-W. Lee, Mechanical properties of supersonic-impacted Al6061 powder particles, *Scr. Mater.* 171 (2019) 52–56.
- [35] A.T. Ernst, M. Wei, M. Aindow, FIB milling strategies for TEM sample preparation of spheroidal powder particles, *Microsc. Microanal.* 24 (Suppl. 1) (2018) 826–827.
- [36] S. Vijayan, B.A. Bedard, M.A. Gleason, H.R. Leonard, D.L. Cote, M. Aindow, Studies of thermally activated processes in gas-atomized Al alloy powders: in situ STEM heating experiments on FIB-cut cross-sections, *J. Mater. Sci.* 54 (2019) 9921–9932.
- [37] I.M. Ritchie, J.V. Sanders, P.L. Weickhardt, Oxidation of a dilute aluminum magnesium alloy, *Oxid. Met.* 3 (1971) 91–101.
- [38] B. Goldstein, J. Dressler, Growth of MgO films with high secondary electron emission on Al-Mg alloys, *Surf. Sci.* 71 (1978) 15–26.
- [39] H.P. Leighly Jr., A. Alam, The oxidation of dilute alloys of magnesium in aluminum, *J. Phys. F: Met. Phys.* 14 (1984) 1573–1583.
- [40] D.J. Field, G.M. Scamans, E.P. Butler, The high temperature oxidation of Al-4.2 Wt Pt Mg alloy, *Metal. Trans. A* 18A (1987) 463–472.
- [41] M.H. Zayan, O.M. Jamjoon, N.A. Razik, High-temperature oxidation of Al-Mg alloys, *Oxid. Met.* 34 (1990) 323–333.
- [42] C.R. Werrett, D.R. Pyke, A.K. Bhattacharya, XPS studies on oxide growth and segregation in aluminum-silicon alloys, *Surf. Interface Anal.* 25 (1997) 809–816.
- [43] A. Nylund, K. Mizuno, I. Olefjord, Influence of Mg and Si on the oxidation of aluminum, *Oxid. Met.* 50 (1998) 309–325.
- [44] H. Nie, M. Schoenitz, E.L. Dreizin, Oxidation of differently prepared Al-Mg alloy powders in oxygen, *J. Alloys Compd.* 685 (2016) 402–410.
- [45] N. Bandaru, D. Ajmera, K. Manwani, S. Majhi, E. Panda, Microstructural analysis of multi-phase ultra-thin oxide overgrowth on Al-Mg alloy by high resolution transmission electron microscopy, *Trans. Indian Inst. Met.* 70 (2017) 1269–1275.
- [46] G. Wu, K. Dash, M.L. Galano, K.A.Q. O'Reilly, Oxidation studies of Al alloys: Part II Al-Mg alloy, *Corr. Sci.* 155 (2019) 97–108.
- [47] Y.-O. Yoon, S.-H. Ha, B.-H. Kim, H.K. Lim, Experimental investigation of MgAl₂O₄ spinel formation in oxidation of Al-Mg alloys, in: A.A. Tomsett (Ed.), Light Metals 2020. The Minerals, Metals & Materials Book Series, Springer, 2020.
- [48] L.P.H. Jeurgens, W.G. Sloof, F.D. Tichelaar, E.J. Mittemeijer, Structure and morphology of aluminum-oxide films formed by thermal oxidation of aluminum, *Thin Solid Films* 418 (2002) 89–101.
- [49] L.P.H. Jeurgens, W.G. Sloof, F.D. Tichelaar, E.J. Mittemeijer, Growth kinetics and mechanisms of aluminum-oxide films formed by thermal oxidation of aluminum, *J. Appl. Phys.* 92 (2002) 1649–1656.
- [50] I. Ganesh, A review of magnesium aluminate (MgAl₂O₄) spinel: synthesis, processing and applications, *Int. Mater. Rev.* 58 (2013) 63–112.
- [51] Z.A. Munir, Analytical treatment of the role of surface oxide layers in the sintering of metals, *J. Mater. Sci.* 14 (1979) 2733–2740.
- [52] R.N. Lumley, T.B. Sercombe, G.B. Schaffer, Surface oxide and the role of magnesium during the sintering of aluminum, *Metall. Mater. Trans. A* 30A (1999) 457–463.
- [53] K. Kondah, A. Kimura, R. Watanabe, Effect of Mg on sintering phenomenon of aluminium alloy powder particle, *Powder Metall.* 44 (2) (2001) 161–164.
- [54] P. Xu, Y. Feng, B. Xu, F. Chen, Y. Lin, Disruption of oxide films during spark plasma sintering of micrometric-sized Al powders and its effect on microstructure and tensile properties of the consolidated Al, *J. Alloys Compd.* 712 (2017) 822–832.
- [55] J. Lienhard, C. Crook, M.Z. Azar, M. Hassani, D.R. Mumm, D. Veysset, D. Apelian, K.A. Nelson, V. Champagne, A. Nardi, C.A.L. Valdevit, Schuh, Surface oxide and hydroxide effects on aluminum microparticle impact bonding, *Acta Mater.* 197 (2020) 28–39.